

Near-infrared polarimetry as a tool for testing properties of accreting super-massive black holes

M. Zamaninasab^{1,2*}, A. Eckart^{2,1}, M. Dovčiak³, V. Karas³, R. Schödel⁴, G. Witzel², N. Sabha², M. García-Marín², D. Kunneriath^{2,1}, K. Mužić⁵, C. Straubmeier², M. Valencia-S^{2,1} and J.A. Zensus^{1,2}

¹Max-Planck-Institut für Radioastronomie, Auf dem Hügel 69, 53121 Bonn, Germany

²I. Physikalisches Institut, Universität zu Köln, Zùlpicher Str.77, 50937 Köln, Germany

³Astronomical Institute, Academy of Sciences, Bořní II 1401, CZ-14131 Prague, Czech Republic

⁴Instituto de Astrofísica de Andalucía - CSIC, Glorieta de la Astrónoma S/N, 18008 Granada, Spain

⁵University of Toronto, Dept. of Astronomy and Astrophysics 50 St. George St. Toronto, ON M5S 3H4, Canada

Accepted 2010 December 1.

ABSTRACT

Several massive black holes exhibit flux variability on time scales that correspond to source sizes of the order of few Schwarzschild radii. We survey the potential of near-infrared and X-ray polarimetry to constrain physical properties of such black hole systems, namely their spin and inclination. We have focused on a model where an orbiting hot spot is embedded in an accretion disk. A new method of searching for the time-lag between orthogonal polarization channels is developed and applied to an ensemble of hot spot models that samples a wide range of parameter space. We found that the hot spot model predicts signatures in polarized light which are in the range to be measured directly in the near future. However, our estimations are predicted upon the assumption of a Keplerian velocity distribution inside the flow where the dominant part of the magnetic field is toroidal.

We also found that if the right model of the accretion flow can be chosen for each source (e.g. on the basis of magnetohydrodynamics simulations) then the black hole spin and inclination can be constrained to a small two-dimensional area in the spin-inclination space. The results of the application of the method to the available near-infrared polarimetric data of Sgr A* is presented. It is shown that even with the currently available data the spin and inclination of Sgr A* can be constrained. Next generations of near-infrared and X-ray polarimeters should be able to exploit this tool.

Key words: black hole physics: general, infrared: general, accretion, accretion disks, Galaxy: centre, Galaxy: nucleus

1 INTRODUCTION

The high-frequency emission from black-hole systems originates mostly close to the black-hole horizon. In this central engine, huge amount of gravitational potential energy is released from gas falling into the black hole. It is known that this emission can vary extremely rapidly (e.g. see Gaskell et al. 2007). This variable emission from compact objects has been interpreted by several authors as being related to the presence of orbiting spots in the inner parts of the accretion flows (Karas & Bao 1992; Karas 1999; Shahbaz 1999; Stella & Vietri 1999; Dovčiak et al. 2004; Schnittman et al. 2006; Broderick & Loeb 2006; Zamaninasab et al. 2010). Here we

will focus on a new method based on the high-frequency time-resolved polarimetric observations which can constrain the intrinsic parameters of the sources.

In the case of stellar-mass black hole candidates, the resemblance between the quasi-periodic oscillation (QPO) time scales and the dynamical frequencies of the black holes near their innermost stable circular orbit (ISCO) has inspired the *hot spot* model (Stella & Vietri 1998, 1999). An orbiting blob inside the accretion flow will produce observable effects in both total and polarized flux. In the case of super-massive black holes, the situation is even more challenging because the measured fluxes are much lower and time scales are much longer. Nonetheless, it is expected that similar physical mechanisms act in both categories of accreting black holes and, after appropriate rescaling, can be

* E-mail: zamani@mpifr-bonn.mpg.de

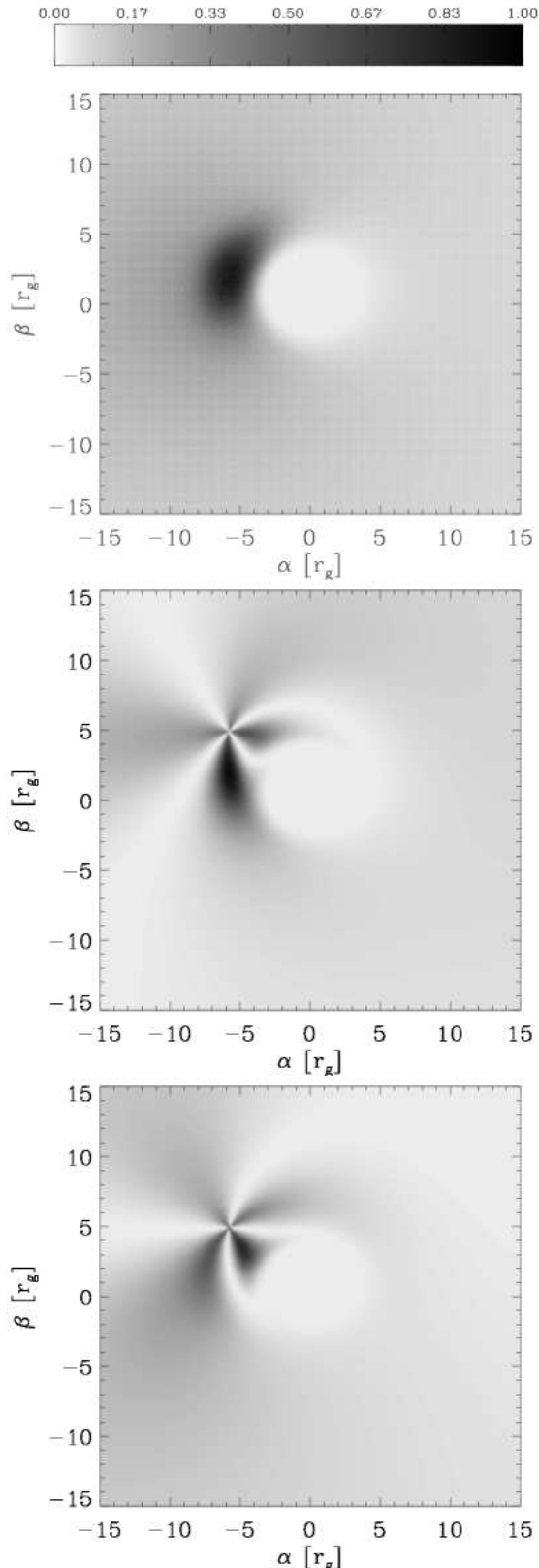


Figure 1. Apparent images of an orbiting spot inside the accretion flow around a Kerr black hole with the spin $a = 0.5$ viewed by an observer inclined by 35° . The image on top shows the ray-tracing output for the total flux, while the middle and bottom show the flux in the 0° and 90° polarization channels, respectively. Here we have assumed that the projected spin axis is aligned toward the north on the observer’s sky ($\theta = 0^\circ$)

considered by similar techniques (Karas and Matt 2007). In Zamaninasab et al (2010), we have discussed in detail how flux magnification and changes in polarization angle (degree) follow specific patterns in this scenario, and we probed such a pattern in a sample of the near-infrared (NIR) flares of Sgr A*.

Several mechanisms have been proposed for the creation of the hot spots, including the random variations resulted from magnetic turbulence inside the magnetohydrodynamics (MHD) flow (Balbus & Hawley 1991, Armitage & Reynolds 2003), vortices and flux tubes (Abramowicz et al. 1992), magnetic flares (Poutanen & Fabian 1999, Zycki 2002) or star-disk interactions (Nayakshin et al. 2004, Dai et al. 2010). It is also shown that multi-component spot scenarios are able to reproduce the overall behaviour of the observed power spectral densities (PSDs) and their (transient) QPO features (Schnittman et al. 2006, Pecháček et al. 2008, Zamaninasab et al. 2010).

In this paper, we will discuss a straightforward method which can be used for constraining the physical parameters of black holes (or other compact objects) which show variable polarized activity. The new method has several advantages in comparison with previous works (Meyer et al. 2006a,b, 2007, Hamaus et al. 2009, Zamaninasab et al. 2008a,b, 2010). We must note that this method, in its core, assumes that variabilities in the flux are caused by orbiting spots. Normally, it has been reported in the literature, that such spots happen to be located at the ISCO. Here we will consider other possibilities for the spot’s location and show how they will affect the predictions of the model (see Dovčiak et al. 2004, Broderick & Loeb 2006 and Reid et al. 2008 for detailed discussion about the spot model and effect of the position of the spot on the observed signal). We must also stress that the results derived here are dependent on our assumptions about the Keplerian velocity of the flow and the magnetic field orientation.

In section 2 we will describe how the spot model predicts a time-lag between orthogonal polarization channels and study how these time-lags are characterized by the black hole mass, spin and inclination angle. A description about the available NIR data from the Galactic Centre black hole and how they can be used to constrain its spin and inclination is provided in section 3. We also briefly discuss a possible way to apply this method to other sources, like RE J1034+396. In section 4, we summarize the main results and draw our conclusions.

2 TIME DELAY BETWEEN POLARIZATION CHANNELS: PREDICTIONS OF THE HOT SPOT MODEL

MHD simulations have demonstrated that in the inner parts of the accreting plasmas, magnetic-field dissipation moderates the field intensity far below its equipartition value (Kowalenko & Melia 1999). Nevertheless, when the gas propagates and follows a Keplerian flow, a MHD dynamo can generate an increased (yet subequipartition) magnetic field that is dominated by its azimuthal component (Hawley, Gammie, & Balbus 1996). In this paper we examine fluctuations occurring in the inner parts of the black hole’s accretion flow, very close to the event horizon. Since our focus

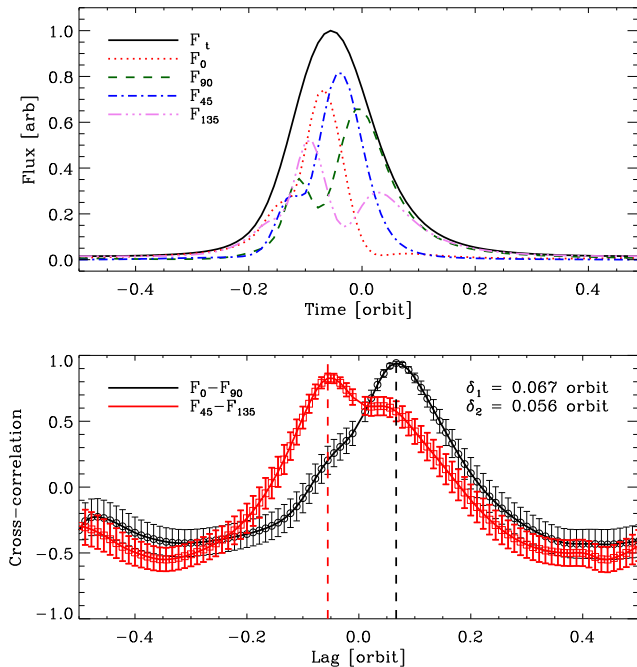


Figure 2. Top: Total flux magnification and the corresponding polarization channels for a spot orbiting at the marginally stable orbit of a Schwarzschild black hole and viewed by an observer inclined by 60° . Flux densities are all normalized to the maximum of the total flux value. Bottom: Cross-correlation between light curves of orthogonal channels: 0° & 90° (black) and 45° & 135° (red). The cross-correlation shows a clear delay between orthogonal pairs of channels with the values of δ_1 and δ_2 . Here we have assumed that the projected spin axis is aligned toward the north on the observer's sky ($\theta = 0^\circ$)

is mainly on radii smaller than $40 r_g$ (where $r_g = \frac{GM}{c^2}$ is the gravitational radius) we have adopted a thin disk approximation while magnetic field is dominated by its azimuthal component. Thin disk approximation was also chosen for reasons of practicability. It allows in a straight forward way (low computational effort) to repeat simulations for a wide range of free-parameters space. Adopting a relativistic treatment of the inner Keplerian region, while considering certain aspects of earlier hydrodynamical simulations, we end up with a model where the gas circulates at small radii twisting the magnetic field inside a relativistic Keplerian disk. To estimate the possible structure of the gas distribution within several Schwarzschild radii of the black hole, we followed the investigation done by Qian et al. (2009).

For the radiation mechanism, we assumed that NIR and X-ray synchrotron photons originate from the relativistic electrons gyrating around magnetic-field lines inside the flow (see Liu et al. 2006, Eckart et al. 2004, 2006, 2008, Zamaninasab et al. 2010). The energy distribution of electrons is approximated by a power-law function:

$$N(\gamma) = \begin{cases} N_0 \gamma^{-p} & \gamma \leq \gamma_c \\ 0 & \gamma > \gamma_c \end{cases} \quad (1)$$

where $N(\gamma)$, γ and γ_c are electron energy distribution function, Lorentz factor of the electrons and its cut-off, respec-

tively. Thus we can define both the ordinary and extraordinary emission coefficients for each point of the accretion disk (Pacholczyk 1970; see also Zamaninasab et al. 2010):

$$\epsilon_\nu^\pm = \frac{\sqrt{3}e^3}{8\pi m_e c^2} N_0 B \sin \theta_e \int \gamma^{-p} [F(x) \pm G(x)] d\gamma \quad (2)$$

where

$$F(x) = \int_x^\infty K_{5/3}(z) dz \quad (3)$$

$$G(x) = x K_{2/3}(x) \quad (4)$$

$$x = \frac{4\pi m_e^3 c^5 \nu}{3eB \sin \theta_e \gamma^2} \quad (5)$$

$K_{5/3}$ and $K_{2/3}$ are the corresponding modified Bessel functions, ν is the frequency measured in the co-moving frame, B is the magnetic-field strength, and θ_e is the angle between the direction of the magnetic field and the direction toward the co-moving observer:

$$\cos(\theta_e) = \sqrt{\frac{(B^\alpha p_{e\alpha})^2}{(p_e^\beta p_{e\beta})(B^\gamma B_\gamma)}} \quad (6)$$

In the above equation B is the magnetic field four-vector and p_e represents the direction of the emitted photon momentum in the co-moving frame.

Since the majority of the high-frequency photons originate from plasma very close to the black hole, the curved structure of space-time must be taken into account. In our simulations, we have used Karas-Yaqoob (KY) code for the ray-tracing (see Dovčiak et al. 2004 for details of the ray-tracing method). Light bending, aberration, Doppler boosting, and frame dragging affect both flux and polarization properties of the emission. The KY code is able to calculate all the relevant relativistic effects for the Kerr space-time. The observed flux density from the accretion disc at a certain observed frequency, F_{ν_o} , can be computed as follows (Dovčiak et al. 2004b, 2008a,b):

$$F_{\nu_o} = \frac{1}{D^2} \int_A G(r, \phi) I_\nu dA \quad (7)$$

where I_ν is the intensity, D is the distance to the source, $dA = r dr d\phi$ is an area element on the disk and $G(r, \phi)$ is the transfer function which contains all the above mentioned relativistic effects. This function depends on the location of the emitter in the disc.

The hot spot is modelled as an over-density of non-thermal electrons centred at a point orbiting at the Keplerian velocity with a Gaussian profile as measured in the co-moving frame:

$$n = n_0 \exp\left[\frac{-(\Delta r)^2}{2R_{spot}^2}\right], \quad (8)$$

where $\Delta r = |\vec{r} - \vec{r}_{spot}|$ with \vec{r}_{spot} being the vector pointing to the centre of the spot. We have chosen the typical value size of one Schwarzschild radius for the size of the spots. For the underlying steady accretion flow, we assumed that both non-thermal electron density and the magnetic field strength scale as r^{-1} . Since our analysis is focused on high-frequency regimes (NIR and X-ray), we have ignored radiative-transfer effects.

Here we must note that some models propose strong deviations from Keplerian velocity for the accretion flow.

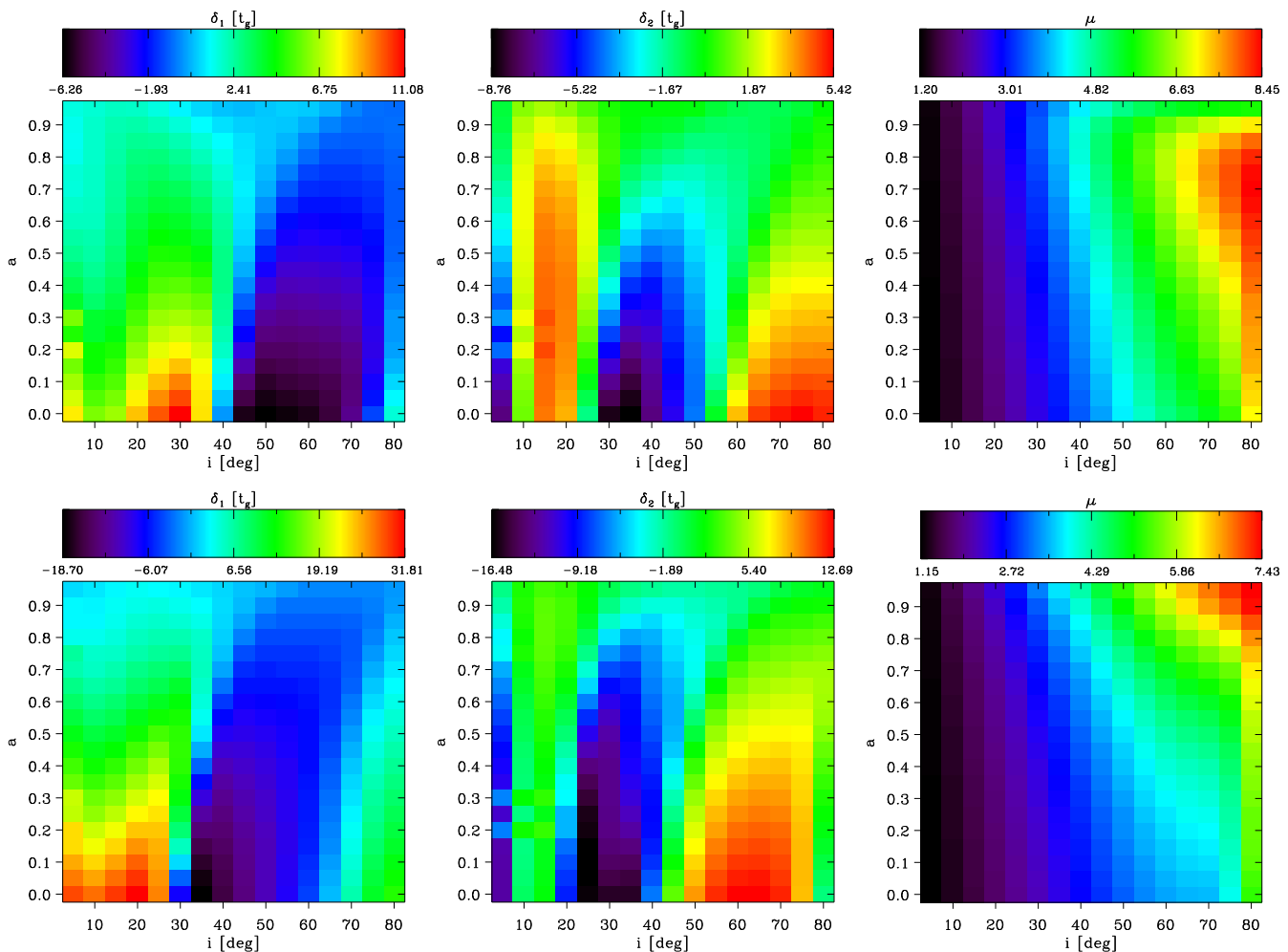


Figure 3. Time lag between the orthogonal polarization channels δ_1 ($\equiv \delta_{0-90}$), δ_2 ($\equiv \delta_{45-135}$) and flux magnification μ , as functions of spin and inclination (from left to right, respectively). The top row corresponds to $\xi = 1.0$ while the bottom row shows the same plots for $\xi = 1.5$. Here we have assumed that the projected spin axis is aligned toward the north on the observer’s sky ($\theta = 0^\circ$). Values are presented in gravitational unit time scale (t_g).

In the absence of an unambiguous theory for the accretion model, we have adopted the simple case of the Keplerian velocity distribution. While our choice of a thin accretion disk reduced the computational time needed for the ray-tracing simulations and made it possible to cover a wide range of free parameters in a reasonable time, it can produce large discrepancies at high inclinations. For this reason, we have limited ourselves to inclinations less than 80° . The dimensionality of the spot is also important for polarized ray-tracing along strongly lensed rays. In this case, many different magnetic field orientations could be encountered (as seen by an observer who is parallel propagating his orientation along the rays). For high spin values this can produce substantial depolarization. Our comparison with three-dimensional simulations with the same setup, showed that for inclinations less than 75° and black hole spin below 0.9 the deviations of the models are less than 15% while above this values it can reach as high as 40%.

Figure 1 shows the images of the assumed accretion flow at an ideal detector as well as polarimetric images at 0° and 90° polarization channels for a spinning black hole

($a = 0.5$) viewed by an observer inclined by 35° . α and β are the projections of the impact parameter of the emitted photons onto the sky. Here we have assumed that the projected spin axis of the black hole coincides with the north on the observer’s sky. We have used these images to extract light curves of the total flux and the corresponding polarization channels. Figure 2 shows the behaviour of flux light curves in 4 orthogonal polarization channels (namely 0° , 45° , 90° and 135° channels) for an orbiting blob located at the ISCO of a Schwarzschild black hole, viewed by an observer inclined by 60° . One can see clearly that each channel reaches its maximum at a different time. The reason for this behaviour is the strong Doppler beaming as well as the light focusing. Furthermore, the rotation of the polarization plane along the photon trajectory plays a role. The latter effect is particularly strong for small radii of the spot orbit (Dovčiak et al. 2008a,b). As Fig. 2 shows, the time-lag between each orthogonal pair of polarization channels can be measured by cross-correlating the corresponding light curves. One can define another parameter called *magnification factor* (μ) which provides useful information about the properties of a light

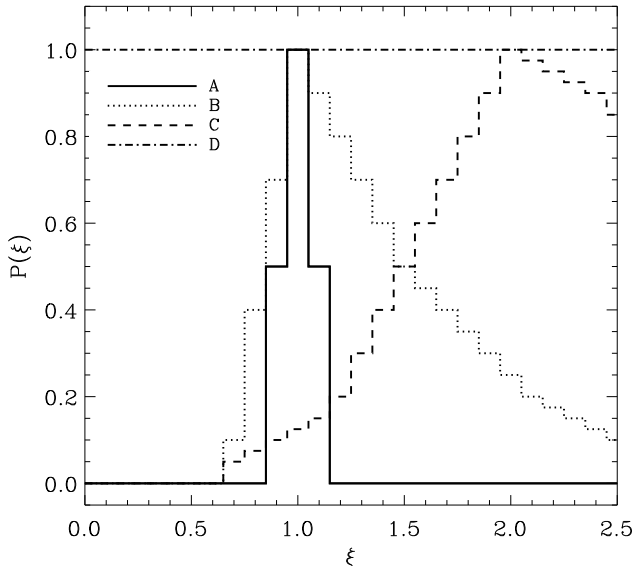


Figure 4. Normalized probability of creation of spots inside the accretion disk as a function of distance from the black hole (ξ). Different curves correspond to different models: (A) spots always created very close to the ISCO, (B) dominant creation happens at ISCO and gradually decreases with increasing radius, (C) maximum probability happens at $2 \times \text{ISCO}$ and (D) equal probability everywhere inside the disk.

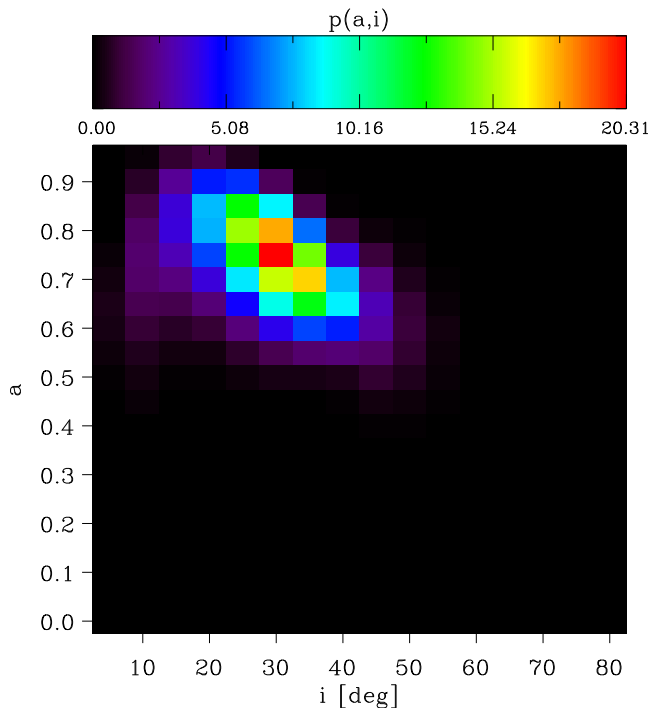


Figure 5. Probability densities for a given inclination and black hole spin marginalised over θ for the hypothetical values of $\delta_1 = (4 \pm 0.5) t_g$, $\delta_2 = (3 \pm 0.5) t_g$ and $\mu = (4 \pm 1)$. This example shows how high accuracy measurements of time-lags and magnification can result in tight constraints on a and i .

curve. Here, the magnification factor refers to the ratio of the maximum flux density to its quiescent value. This factor is a measure of how much the flux is magnified by lensing and boosting effects.

Up to here, we assumed that the projected spin axis of the black hole is aligned toward the north on the observer's sky. In general, the measured time-delay between two orthogonal polarization channels depends on the orientation of the projected spin axis with respect to the north (θ , vanishing at the north and increasing toward the east) in our chosen reference coordinates. In order to reduce this dependency, one can measure simultaneously time delays between two pairs of orthogonal channels which are rotated by 45° with relative to one another. Since changing the position angle corresponds simply to a coordinate rotation, the images were originally computed only for a single position angle, namely $\theta = 0^\circ$. The time-lag associated with each desired value of θ were extracted from these images by applying the appropriate Mueller matrices.

The main question which rises in this step is how these time lags ($\delta_1 \equiv \delta_{0-90}$ and $\delta_2 \equiv \delta_{45-135}$) and magnification factor (μ) are sensitive to the changes of the global parameters of our model. The main free parameters are the spin of the black hole ($0 \leq a \leq 1$ in geometric dimensional units), inclination of the observer ($0^\circ \leq i \leq 90^\circ$, when the edge-on view corresponds to $i = 90^\circ$), orientation of the projected spin axis on the sky ($-90^\circ \leq \theta \leq 90^\circ$, vanishing at the north and increasing toward the east), and the distance of the blob from the black hole (controlled by the parameter ξ ; $r_{sp} = \xi \times \text{ISCO}$). Figure 3 shows δ_1 , δ_2 and μ as functions of the spin and inclination for a black hole of the mass M in gravitational units. The functions have been presented for two distances of the spot from the black hole ($\xi = 1.0$ and $\xi = 1.5$) while $\theta = 0^\circ$. We have calculated these functions for a wide range of acceptable values of this parameter ($\xi = 0.5 - 3.0$; with a step of 0.1). One can see that these three different functions behave differently in the $a-i$ space. This allows us to use these functions as tools for constraining spin, inclination and orientation of the accreting systems.

It is clear from Fig. 3 that our results are sensitive to the exact location of the orbiting blob with respect to the black hole (see predictions for $\xi = 1.0$ and $\xi = 1.5$ in Fig. 3). Unfortunately, there is no direct way to constrain that parameter. A lot of effort have been devoted to understand where the radiation and the stress edges of an accretion disk are located and how they depend on the different assumptions of the models (Beckwith et al. 2008, Shafee et al. 2008, Hilburn et al. 2010, Noble et al. 2009, 2010). Since it is not yet clear how and where spots can be created inside an accretion disk, we have assumed four different types of models for the spatial distribution of the spots as a function of distance from the black hole (Fig. 4). We have considered models in which the main creation of spots happens only around the ISCO (model A), distributed over the disk with the maximum at the ISCO and gradually decreases with increasing the radius (model B), distributed over the disk with the maximum at the $2 \times \text{ISCO}$ (model C, see Shafee et al. 2008) and an equal distribution for the probability of a spot being located anywhere inside the disk (model D). We have used the product of the magnetic stress and energy dissipation functions from MHD simulations (e.g. Hilburn et al. 2009 and Shafee et al. 2008) in order to define such

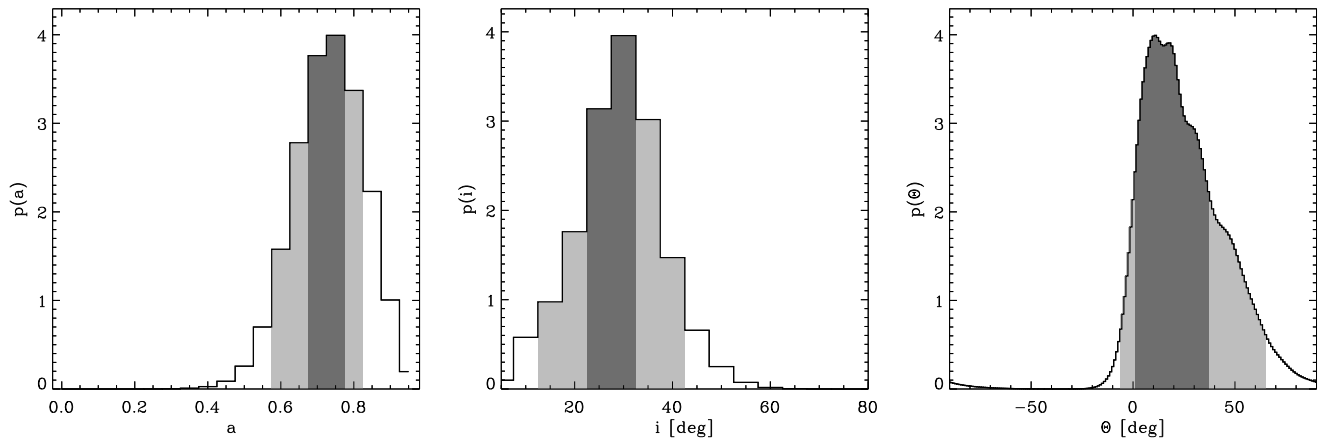


Figure 6. Probability densities for a given spin $p(a)$, inclination $p(i)$ and orientation of the system on the sky $p(\theta)$, marginalised over other parameters (left to right, respectively). The assumed values of δ_1 , δ_2 and μ are the same as in Fig. 5. The dark and light shaded areas denote the 1σ and 2σ confidence limits, as defined in the text, respectively.

radial distributions. We have adopted a Bayesian parameter estimation method used by Broderick et al. 2009. Here, we repeat the basics of the method in order to keep the paper self-contained (see Broderick et al. 2009 for more details about the method).

The constraints upon a , i and θ we report here, suffer from the uncertainty introduced by the assumption that our model is appropriate for the observations. We compute the probability following a Bayesian scheme, which states that a given set of model parameters (a, i, θ) are correct for the measured delays and magnifications.

Given a particular set of model parameters (a, i, θ, ξ) , the probability of measuring an observable x_j (where $x_j \in [\delta_{1j}, \delta_{2j}, \mu_j]$), assuming Gaussian observational errors, is

$$P_j(x_j|a, i, \theta, \xi) = \frac{1}{\sqrt{2\pi}\Delta x_j} \exp\left\{-\frac{[x_j - x(a, i, \theta, \xi)]^2}{2\Delta x_j^2}\right\} dx_j. \quad (9)$$

Therefore, the probability of simultaneously observing a measured set of $[\delta_{1j}, \delta_{2j}, \mu_j]$ for a certain model is

$$\frac{P(\{\delta_{1j}, \delta_{2j}, \mu_j\}|a, i, \theta, \xi)}{P(\delta_{1j}|a, i, \theta, \xi) \times P(\delta_{2j}|a, i, \theta, \xi) \times P(\mu_j|a, i, \theta, \xi)}. \quad (10)$$

Contrary to eq. (10), which gives the probability that the observed quantities come from a certain model, choosing an appropriate set of priors on a , i , θ and ξ allows us to compute, via Bayes' theorem, the probability density of a set of model parameters given the observed values, i.e. $p(a, i, \theta, \xi|\{x_i\})$. As such, we now turn to the problem of choosing these priors.

Assuming the isotropic probability of the black hole's spin orientation, a choice for the prior upon i and θ can be made so that $\varphi(i, \theta) = \sin(i)$ (Broderick et al. 2009). The prior on a is chosen to be uniform, i.e. $\varphi(a) = 1$ since we lack a complete theoretical knowledge about the spin evolution of super-massive black holes. Finally, the prior on ξ is set according to the models in Figure 4. Therefore, Bayes' theorem gives

$$\begin{aligned} p(a, i, \theta, \xi|\{x_j\}) &= \frac{P(\{x_j\}|a, i, \theta, \xi)\varphi(a)\varphi(i, \theta)\varphi(\xi)}{\int da di d\theta d\xi P(\{x_j\}|a, i, \theta, \xi)\varphi(a)\varphi(i, \theta)\varphi(\xi)} \quad (11) \\ &= \frac{P(\{x_j\}|a, i, \theta, \xi) \sin(i)}{\int da di d\theta d\xi P(\{x_j\}|a, i, \theta, \xi) \sin(i)}. \end{aligned}$$

As it can be seen, this is a probability density in a four-dimensional parameter space, which makes it difficult to be visualized directly. Therefore, we construct a variety of marginalised probabilities for presentation and analysis. This is done by forming a pair of two-dimensional $p(a, i)$ function with the probability densities marginalised over θ and ξ :

$$p(a, i) = \int d\theta d\xi p(a, i, \theta, \xi|\{x_j\}) \quad (12)$$

This is plotted in Fig. 5 for a hypothetical example of a source with the measured delays of $\delta_1 = (4 \pm 0.5) t_g$ (where t_g is the gravitational time) and $\delta_2 = (3 \pm 0.5) t_g$ while the flux is magnified by a factor of $\mu = (4 \pm 1)$. In an observationally-constrained astrophysical case, it is difficult to determine the values of the time delays and magnification so precisely. As one can see, the model allows to exclude a wide range of possible a - i combinations and well constrains the possible range of inclination and black hole's spin. In order to distinguish the probability distribution of each parameter, the marginalised one-dimensional probability densities are also constructed:

$$p(a) = \int d\theta di d\xi p(a, i, \theta, \xi|\{x_j\}) \quad (13)$$

$$p(i) = \int d\theta da d\xi p(a, i, \theta, \xi|\{x_j\}) \quad (14)$$

$$p(\theta) = \int di da d\xi p(a, i, \theta, \xi|\{x_j\}). \quad (15)$$

These are shown in Fig. 5 for the same hypothetical values of δ_1 , δ_2 and μ as in Fig. 6. For both Figs. 5 and 6 we have used

the commonly used assumption that the spot is located at the ISCO (model A for $p(\xi)$). It is evident that the allowed parameter space is highly non-Gaussian. As a result, the extraction of values and their associated uncertainties for the fitting parameters must be done carefully. These values will be highly correlated in all occurrences, and the systematic uncertainties due to assuming a particular accretion model will dominate the errors (and thus will not be reviewed again here).

For determining the 1σ and 2σ error intervals, we used an additive probability as defined in Broderick et al. 2009:

$$P(> p) = \int_{p(\mathbf{x}) \geq p} p(\mathbf{x}) d\mathbf{x} \quad (16)$$

where \mathbf{x} is the parameter of the total probability distribution. The above definition of $P(> p)$ gives the probability associated with the parameter space region that has a probability density above p . We set the $1\text{-}\sigma$ and 2σ contours to indicate the regions of p for which $P(> p) = 0.683$ and $P(> p) = 0.954$, respectively. These follow the normal definition of 1σ and 2σ errors, while in our case the errors are strongly non-Gaussian. In Fig. 6 the 1σ and 2σ confidence intervals are indicated by the dark and light shaded regions.

In the next section, we will discuss the implications of our model for the observed variable NIR polarized emission from Sagittarius A*.

3 OBSERVATIONS

3.1 Near-Infrared Flares of Sagittarius A*

At the centre of the Milky Way stellar motions allow us to firmly associate Sagittarius A* (Sgr A*) with a $\sim 4 \times 10^6 M_\odot$ super-massive black hole (Eckart & Genzel 1996, Genzel et al. 1997, 2000, Ghez et al. 1998, 2000, 2003, 2005a, 2008, Eckart et al. 2002, Schödel et al. 2002, 2003, 2009, Eisenhauer et al. 2003, 2005, Gillessen et al. 2009).

Recent radio, near-infrared and X-ray observations have detected variable and polarized emission and give detailed insight into the physical emission mechanisms at work in Sgr A* (e.g. Baganoff et al. 2001, 2002, 2003, Eckart et al. 2002, 2004, 2006, 2008, 2009, Porquet et al. 2003, 2009, Goldwurm et al. 2003, Genzel et al. 2003, Reid et al. 2004, Ghez et al. 2004ab, Eisenhauer et al. 2005, Belanger et al. 2006, Hornstein et al. 2007, Yusef-Zadeh et al. 2006ab, 2007, 2008, 2009, Marrone et al. 2008, Sabha et al. 2010). Sgr A* - in terms of Eddington luminosity - is the faintest super-massive black hole known. However, due to its proximity it is bright enough to be studied in great detail. With the possible exception of the closest galaxies, no extragalactic super-massive black hole with a similar feeble Eddington rate would be observable.

The NIR data we investigate here were taken in the K_s band with the NIR camera CONICA and the adaptive optics (AO) module NAOS (NACO) at the ESO VLT unit telescope 4 (YEPUN) on Paranal, Chile¹ on 13 June 2004

¹ Based on observations at the Very Large Telescope (VLT) of the European Southern Observatory (ESO) on Paranal in Chile; Programs:075.B-0093 and 271.B-5019(A).

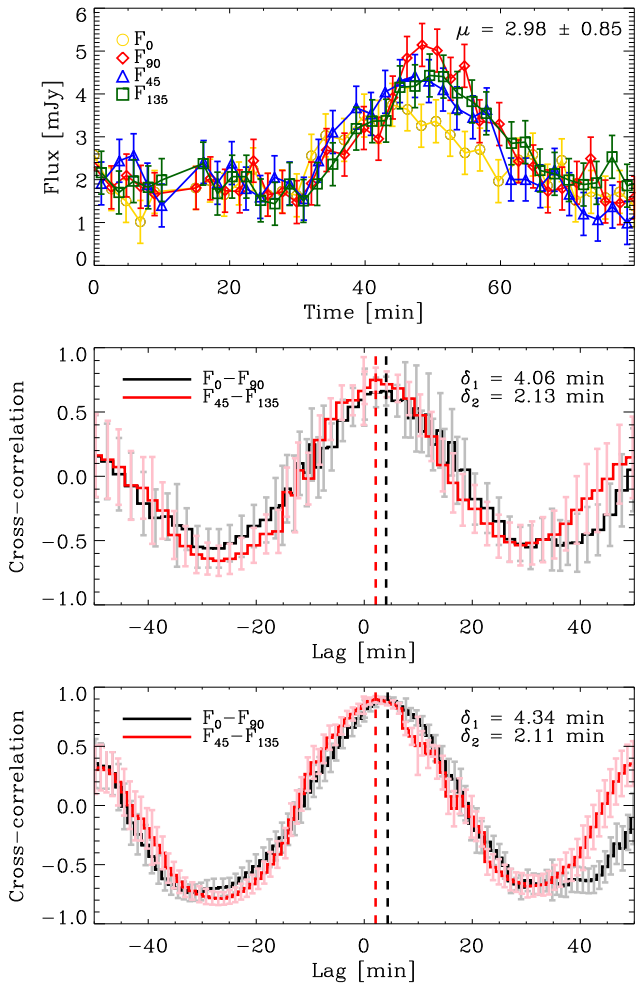


Figure 7. The NIR flare event of Sgr A* observed on 13 June 2004. Four different polarized channels are indicated with different colours (top). In order to derive the time-lags a cross-correlation analysis has been performed. Maximum of two cross-correlation curves have been indicated with two different methods (middle and bottom). The average values of $\bar{\delta}_1 = (4.20 \pm 1.00)$ min, $\bar{\delta}_2 = (2.12 \pm 1.00)$ min and $\bar{\mu} = (2.98 \pm 1.00)$ derived from both analysis.

(start of observation: 07:20:02 UT). For determining the linear polarization characteristics of a time-varying source, a Wollaston prism, installed on the NACO NIR camera, permits simultaneous measurements of two orthogonal directions of the electric field vector. It is combined with a rotary half-wave plate to allow for rapid alternating measurements of the electric field vector at different angles. Details of the data reduction and flux calibration is described in Eckart et al. (2006a), and Zamaninasab et al. (2010).

Figure 7 shows light curves of a polarized flare from Sgr A* observed on 13 June 2004 in four polarization channels. There is a clear time-lag visible between orthogonal channels which is bigger than the sampling rate of the observations. Furthermore, the light curve is continuous and there is no gap according to the usual sky background measurements at the time of the flare. Each channel shows an approximate Gaussian behaviour while clear time-lags be-

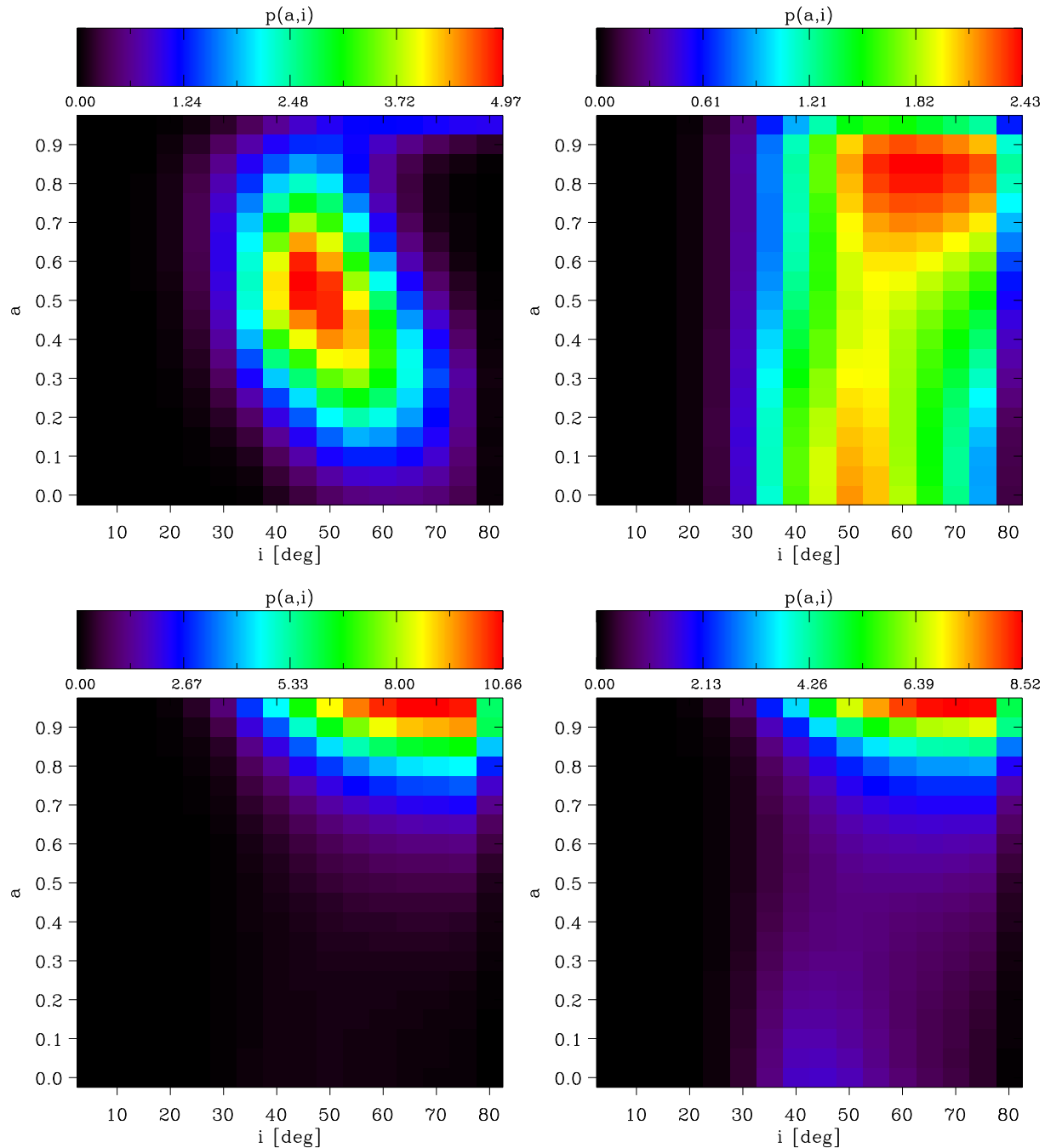


Figure 8. Same as Fig. 5 for the time-lag and magnification values derived from the observed flare of Sgr A* on 13 June 2004 (Fig. 7). The results are shown for different models of $p(\xi)$: model A (top left), model B (top right), model C (bottom left) and model D (bottom right).

tween maxima (specially between orthogonal pairs) are visible.

We have calculated the time lag between orthogonal pair of channels for the original (Fig. 7 middle) and first-order interpolated light curves (Fig. 7 bottom). For the cross-correlation function we have followed Alexander (1997). Results of both methods are well in agreement with each other. This leads to the estimated values of the time delays between orthogonal polarization channels $\bar{\delta}_1 = (4.20 \pm 1.00)$ min, $\bar{\delta}_2 = (2.12 \pm 1.00)$ min and a mag-

nification value of $\bar{\mu} = (2.98 \pm 1.00)$. The errors in these estimations derived from the standard deviation of χ^2 fitting of Gaussian functions to the observed flux and cross-correlation functions. We must note that the sampling rate of this observation was ~ 2 min, so the level of confidence specially for the δ_2 value is not high. In order to improve these estimates we need high SNR images observed in polarimetry with higher time resolutions.

Although the time resolution of the available data is not better than 1.5 minutes, it is good enough to rule out

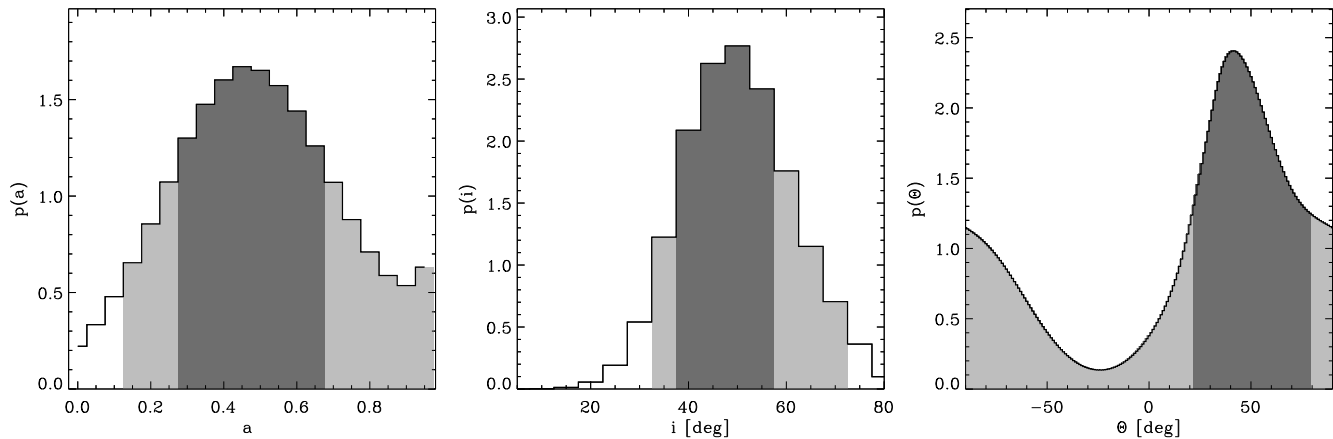


Figure 9. Same as Fig. 6 for the time-lag and magnification values derived from the observed flare of Sgr A* on 13 June 2004 (Fig. 7). $p(a)$, $p(i)$ and $p(\theta)$ are marginalised over all other parameters assuming model A for $p(\xi)$.

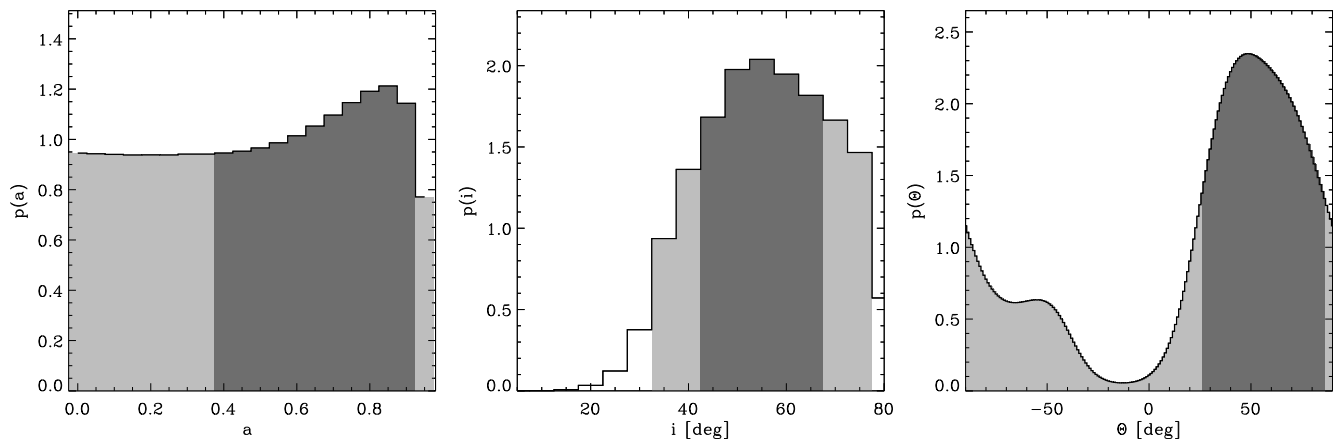


Figure 10. Same as Fig. 9 assuming model B for $p(\xi)$.

some parts of the $a - i$ plane. Fig. 8 shows two-dimensional marginalised probability densities $p(a, i)$ for the measured values of magnification and time delays. The Four different images correspond to different assumptions about the spatial distribution of the spots ($p(\xi)$). We see that while the most popular assumption that spots are located around the ISCO (model A) results in $a = 0.5_{-0.4}^{+0.3}$ and $i = 50_{-20}^{+20}$, the more reasonable assumption which allows the spots to be created over a wider range of locations increases the estimated values for both inclination and black hole's spin.

Figs. 9-12 show the fully marginalised probability distributions for different assumptions about $p(\xi)$, respectively. However, we must remind the reader that these parameter estimates are strongly correlated, and thus they should be used with caution. Here we again use the additive probability, $P(> p)$ to define the 1σ and 2σ intervals, shown in the panels of Figs. 9-12 as the dark and light shaded regions, respectively.

From the left panel of Fig. 9, the most likely spin value is $a = 0.45_{0.15}^{+0.2}$ (1σ confidence). While we can rule out very low spins ($a \leq 0.1$) at the 2σ level for our particular choice of $p(\xi)$, the spin is otherwise weakly constrained. Left panels of Figs. 9-12 show that this estimation is highly dependant

on the choice of $p(\xi)$ and has a tendency toward higher spin values for models B-D.

In contrast, the inclination is robustly limited towards moderate and high angles. The most likely inclination value is $i = 55_{-20}^{+20}$ (1σ confidence). It can be seen clearly in the central panels of Figs. 9-12 that face-on geometries ($i \leq 30^\circ$) are convincingly ruled out. However, the general trend of all the considered models is toward highly inclined systems.

Interestingly, constraining the position angle shows that all the $p(\xi)$ assumptions result in a more or less similar values ($\theta = 50_{-20}^{+30}$) as can be seen in the right panels of Figs. 9-12.

Our limits upon the black hole's spin are in good agreement with previous estimates by Huang et al. 2009, Dexter et al. 2010 and Moscibrodzka et al. 2009 while it contradicts the low spin values favoured by Broderick et al. 2009. However, we remind the reader again that the constraints on spin are not strong enough to rule out any possibility.

The limits upon the inclination are also in quite good agreement with previous efforts (Meyer et al. 2006, Markoff et al. 2007, Broderick et al. 2009, Falanga et al. 2009, Huang et al. 2009, Moscibrodzka et al. 2009 and Dexter et al. 2010). They all favour high inclinations using different approaches to the problem. Falanga et al. 2009, for example, find an in-

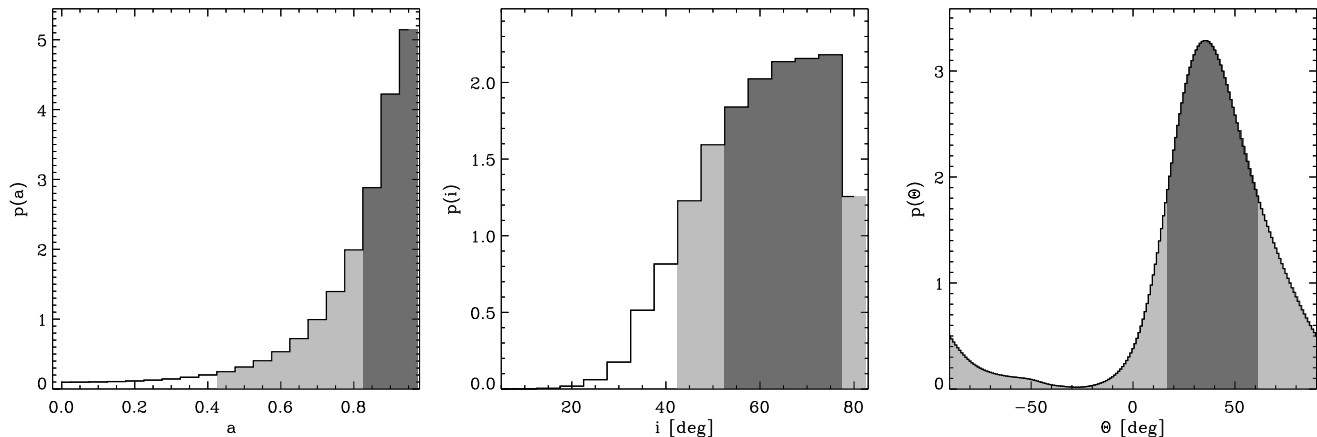


Figure 11. Same as Fig. 9 assuming model C for $p(\xi)$.

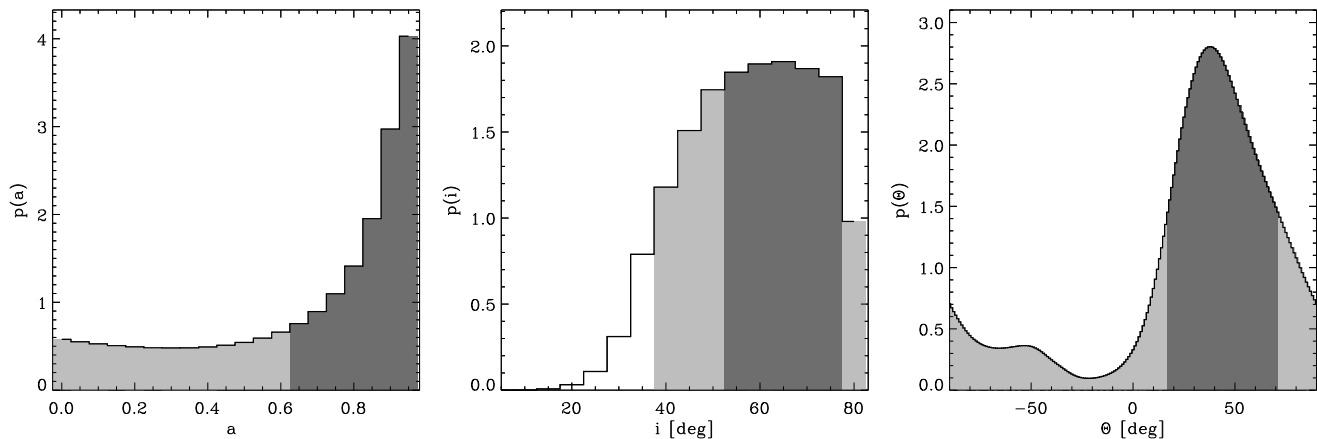


Figure 12. Same as Fig. 9 assuming model D for $p(\xi)$.

clination of about $77^\circ \pm 10^\circ$ (similar to the results by Meyer et al. 2006) by fitting Sgr A*'s flares with a model of hydrodynamic instabilities. On the other hand, Markoff et al. 2007 fit the long-wavelength observations with a different approach, a hydrodynamic jet. They also favour large inclinations ($i \geq 75^\circ$).

Unlike the inclination, our position angle estimate disagrees significantly with many previous efforts except Meyer et al. 2006 and Markoff et al. 2007. Our estimated position angle is marginally consistent with the second solution of Broderick et al. 2009 at the 1σ level.

However, we have noticed that our estimated θ coincides very well with the value derived by Mužić et al. 2010 where they used the structure of two bow shock stars (namely X3 and X7) in the vicinity of Sgr A* to trace a possible outflow scenario (Fig. 13). Our best bet ($\theta = 50^\circ$) exactly passes the positions of X3, X7 and the mini-cavity as shown in Fig. 13. It is proposed that the whole mini-cavity structure can be caused by wind from the direction of Sgr A* implied by traces of hot gas and plasma shocks observed in this region (Yusef-Zadeh et al. 1990, Yusef-Zadeh & Melia 1992, Yusef-Zadeh & Wardle 1993 and Muzic et al. 2007). At the same time, the results leave a lot of space for future improvements.

3.2 The case of RE J1034+396

The main advantage of this method is its applicability for a wide range of compact sources which show polarized variable emission in NIR and X-ray wavelengths. Since the current technical difficulties do not allow for polarimetric observations with time resolutions less than ~ 30 seconds (at least as far as it concerns VLT), the method is currently applicable to sources with masses greater than $\sim 10^6 M_\odot$. This makes objects like RE J1034+396 perfect candidates for testing predictions of the hot spot model. The recent unambiguous discovery of one hour periodicity in the X-ray emission light curve of this source is interpreted to be related to the ISCO frequency of this super-massive black hole (Gierliński et al. 2008). Unfortunately, there is no polarimetric observation of this source available so far. The mass of the object is also not well determined (the estimates vary from 6.3×10^5 to $3.6 \times 10^7 M_\odot$). This source looks to be a promising target for future X-ray polarimetry if its mass estimation can be improved (using reverberation mapping for example).

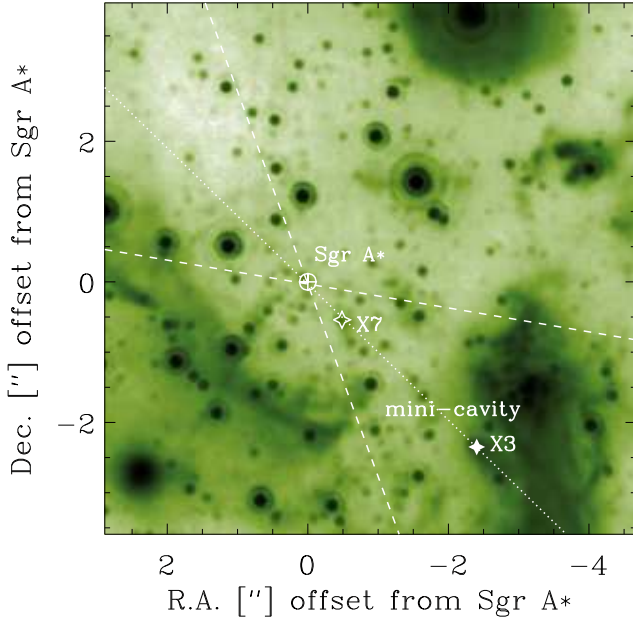


Figure 13. The estimated orientations of the Sgr A*’s spin axis in our sky from all the models of $p(\xi)$ ($\theta = 50_{-20}^{+30}$) are in very well agreement with the study of Muzic et al. 2010 which relates the alignment of two bow shock sources (X3 & X7, marked with open and filled stars respectively) and mini-cavity as a possible hint for a wind from Sgr A*.

4 SUMMARY AND CONCLUSION

We have investigated the general relativistic effects on the polarization properties of the emission from an orbiting spot inside the accretion flow around a black hole. We have described a method in which observing the time delay between the polarization channels in high-frequency regimes can lead to a constraint on the spin and inclination of the black hole. The method may also be applied to the X-ray domain for sources which are bright enough in polarized X-ray flux. We applied the method to several hot spot models that sample a wide range of parameter space. We have discussed how the probability for the spatial distribution of the spots can affect our results. This shows the crucial need for reliable 2 and 3-dimensional GRMHD simulations of accretion disks concerning the exact location of the plunging region and the stress edge. The results of the application of the method to the available NIR polarimetric data of Sgr A* is also presented. The results for this source are consistent with previous findings of an inclined accretion disk around a spinning black hole ($a \geq 0.4$). While with current VLT facilities the rate at which high S/N images in polarized flux density are taken can be increased significantly by a new method of observation, the next generations of NIR and X-ray polarimeters should be able to exploit this method as a powerful probe of the metric around black holes.

ACKNOWLEDGEMENTS

Authors would like to thank the anonymous referee for his/her helpful comments on the paper. Part of this work was supported by the German *Deutsche Forschungsgemein-*

schaft, DFG via grant SFB 494. MZ, DK and MV-S are members of the International Max Planck Research School (IMPRS) for Astronomy and Astrophysics at the MPIfR and the Universities of Bonn and Cologne. NS acknowledges support from the Bonn-Cologne Graduate School of Physics and Astronomy (BCGS). RS acknowledges the Ramón y Cajal program of the Spanish Ministry of Science and Innovation. VK and MD acknowledge the Czech Science Foundation (ref. 205/07/0052).

REFERENCES

- Abramowicz M. A., Lanza A., Spiegel E. A., Szuszkiewicz E., 1992, *Nature* 356, 41-43
 Alexander T., 1997, *ASSL* 218, 163
 Armitage P. J., Reynolds C. S., 2003, *MNRAS* 341, 1041
 Balbus S. A., Hawley J. F., 1991, *ApJ*, 376, 214
 Beckwith K., Hawley J. F., Krolik J. H., 2008, *MNRAS*, 390, 21
 Baganoff F. K., Bautz M. W., Brandt W. N. et al., 2001, *Nature*, 413, 45
 Baganoff F. K. et al., 2002, 201st AAS Meeting, #31.08; *Bulletin of the American Astronomical Society*, Vol. 34, 1153
 Baganoff F. K., Maeda Y., Morris M., et al. 2003, *ApJ* 591, 891
 Belanger G., Terrier R., de Jager O. C., Goldwurm A., Melia F., 2006, *JPhCS* 54, 420
 Broderick, A. E., Fish, V. L., Doeleman, S. S., Loeb, A., 2009, *ApJ* 697, 1, 45
 Broderick A. E., Loeb A., 2006, *MNRAS* 367, 905
 Dai L., Fuerst S. V., Blandford R., 2010, *MNRAS*, 402, 1614
 Devillard N., 1999, *ASPC* 172, 333
 Dexter, J., Agol, E., Fragile, P. C., McKinney, J. C., 2010, *ApJ* 717, 2, 1092
 Dovčiak M., Karas V., Yaqoob T., 2004, *ApJS* 153, 205
 Dovčiak M., Karas V., Matt G., Goosmann R. W., 2008a, *MNRAS* 384, 361
 Dovčiak M., Muleri F., Goosmann R. W., Karas V., Matt G., 2008b, *MNRAS* 391, 32
 Eckart A., Genzel R., 1996, *Nature* 383, 415
 Eckart A., Genzel R., Ott T., Schödel R., 2002, *MNRAS*, 331, 917
 Eckart A., Baganoff F. K., Morris M. et al., 2004, *A&A* 427, 1
 Eckart A., Schödel R., Meyer L. et al., 2006, *A&A* 455, 1
 Eckart A., Baganoff F. K., Zamaninasab M. et al., 2008, *A&A* 479, 625
 Eckart A., Baganoff F. K., Morris M. R. et al., 2009, *A&A* 500, 935
 Eisenhauer F., Schödel R., Genzel R., et al. 2003, *ApJ* 597, L121
 Eisenhauer F., Genzel R., Alexander T., 2005, *ApJ* 628, 246
 Falanga, M., Melia, F., Tagger, M., Goldwurm, A., Belanger, G., 2007, *ApJ* 662, 1, L15
 Gaskell, C. M., McHardy, I. M., Peterson, B. M., & Sergeev, S. G., eds. 2006, *Astronomical Society of the Pacific Conf. Series*, Vol. 360, *AGN Variability from X-Rays to Radio Waves*
 Genzel, T., Eckart, A., Ott, T. & Eisenhauer, *MNRAS* 1997, 291, 219
 Genzel R., Pichon C., Eckart A., Gerhard O.E., Ott T. 2000, *MNRAS* 317, 348
 Genzel R., Schödel R., Ott T. et al., 2003, *Nature*, 425, 934
 Ghez A., Klein B.L., Morris M. & Becklin, E.E. 1998, *ApJ*, 509, 678
 Ghez A., Morris M., Becklin E. E., Tanner A., Kremenek, T., 2000, *Nature* 407, 349
 Ghez A. M., Duchéne G., Matthews K. et al., 2003, *ApJ*, 586, L127
 Ghez A. M., Wright S. A., Matthews K. et al., 2004a, *ApJ* 601, 159

- Ghez A. M., Hornstein S.D., Bouchez A., Le Mignant D., Lu J., Matthews K., Morris M., Wizinowich P., Becklin E. E., 2004b, AAS 205, 2406
- Ghez A. M., Salim S., Weinberg N. N., 2008, 689, 1044
- Gierliński M., Middleton M., Ward M., Done C., 2008, Nature 455, 369
- Gillessen S., Eisenhauer F., Trippe S., et al., 2009, ApJ 692, 1075
- Goldwurm, A., Brion, E., Goldoni, P., Ferrando, P., Daigne, F., Decourchelle, A., Warwick, R. S., Predehl, P., 2003, ApJ 584, Issue 2, 751
- Hamaus N., Paumard T., Müller T. et al., 2009, ApJ 692, 902
- Hawley J. F., Gammie C. F., Balbus S. A., 1996, ApJ 464, 690
- Hilburn, G., Liang, E., Liu, S., Li, H., 2010, MNRAS 401, 3, 1620
- Hornstein S. D., Matthews K., Ghez A. M., et al. 2007 ApJ 667, 900
- Huang, L., Takahashi, R., Shen, Z., 2009, ApJ 706, 2, 960
- Karas V. & Bao G., 1992, A&A 257, 531
- Karas, V. 1999, PASJ, 51, 317
- Karas, V., Matt, G., 2007, Black holes from stars to galaxies across the range of masses : proceedings of the 238th symposium of the International Astronomical Union held in Prague, Czech Republic August 21-25, 2006, Cambridge University Press.
- Kowalenko V., Melia F., MNRAS, 310, 1053
- Liu S., Melia F., Petrosian V., 2006, ApJ 636, 798
- Markoff, S., Bower, G. C., Falcke, H., 2007, MNRAS 379, 4, 1519
- Marrone D. P., Baganoff F. K., Morris M. et al., 2008, ApJ 682, 373
- Meyer L., Eckart A., Schödel R., et al. 2006, A&A 460, 15
- Moscibrodzka, M., Gammie, C. F., Dolence, J. C., Shiokawa, H., Leung, P. K., 2009, ApJ 706, 1, 497
- Mužić, K., Eckart, A., Schödel, R., Meyer, L., Zensus, A., 2007, A&A 469, 3, 993
- Mužić, K., Eckart, A., Schödel, R., Buchholz, R., Zamaninasab, M., 2010, A&A, 521, id.A13
- Nayakshin, S., Cuadra, J., Sunyaev, R., 2004, A&A 413, 173
- Noble S. C., Krolik J. H., Hawley J. F., 2009, ApJ, 692, 411
- Noble S. C., Krolik J. H., Hawley J. F., 2010, ApJ, 711, 959
- Pacholczyk A. G., 1970, *Radio astrophysics: Nonthermal processes in galactic and extragalactic sources*, San Francisco: Freeman
- Pecháček T., Karas V., Czerny B., 2008, A&A 487, 815
- Porquet D., Predehl P., Aschenbach P. et al., 2003, A&A 407, L17
- Porquet D., Grosso N., Predehl P., et al., 2009, A&A 488, 49
- Poutanen J., Fabian A. C., 1999, MNRAS, 306, L31
- Qian L., Abramowicz M. A., Fragile P. C. et al., 2009, A&A, 498, 471
- Reid, M. J., Brunthaler, A., 2004, ApJ 616, Issue 2, 872
- Reid, M. J., Broderick, A. E., Loeb, A., Honma, M., Brunthaler, A., 2008, ApJ 682, 2, 1041
- Sabha N.; Witzel G.; Eckart A. et al., 2010, A&A 512, id.A2
- Shafee R., Narayan R., McClintock J. E., 2008, ApJ, 676, 549
- Shahbaz T., 1999, Journal of Astrophysics and Astronomy, 20, 197
- Schnittman J. D., Krolik J. H., Hawley J. F., 2006, ApJ, 651, 1031
- Stella L., Vietri M., 1998, ApJL, 492, L59
- Stella L., Vietri M., 1999, PRL, 82, 17
- Schödel R., Ott T., Genzel R., et al., 2002, Nature 419, 694
- Schödel R., Genzel R., Ott et al. 2003, ApJ, 596, 1015
- Schödel R., Eckart A., Alexander T., et al. 2007, A&A 469, 125
- Yusef-Zadeh, F., Morris, M., Ekers, R. D., 1990, Nature 348, 1990, 45
- Yusef-Zadeh, F., Melia, F., 1992, ApJL 385, 1992, L41
- Yusef-Zadeh, F., Wardle, M., 1993, ApJ 405, 2, 584
- Yusef-Zadeh F., Bushouse H., Dowell C. D., et al., 2006a, ApJ 644, 198
- Yusef-Zadeh F., Roberts D., Wardle M., Heinke C. O., Bower G. C., 2006b, ApJ 650, 189
- Yusef-Zadeh F., Wardle M., Cotton W. D., Heinke C. O., Roberts, D. A., 2007, ApJ 668, 47
- Yusef-Zadeh F., Wardle M., Heinke C., et al. 2008, ApJ 682, 361
- Yusef-Zadeh F.; Bushouse H.; Wardle M. et al. 2009, ApJ, 706, 348
- Zamaninasab M., Eckart A., Kunneriath D. et al. 2008a, MmSAI 79, 1054
- Zamaninasab M., Eckart A., Meyer L. et al. 2008b, JPhCS 131a
- Zamaninasab M., Witzel G., Eckart A., 2010, A&A, 510, id.A3
- Zycki P. T., 2002, MNRAS, 333, 800

This paper has been typeset from a T_EX/ L^AT_EX file prepared by the author.

